

# Effective controller design for the three-phase cascaded H-bridge multilevel active power filter

**Abstract.** This paper presents the modelling and effective controlled design for the three-phase cascaded H-bridge (CHB) multilevel active power filter (APF). The mathematical model of the CHB-APF is derived using state-space representations, and the discrete domain model is also presented. A robust predictive current controller is proposed, which shows excellent steady-state precision and sufficient dynamic characteristics owing to the Luenberger observer-based adaptive control algorithm. The digital simulation results obtained from the Matlab/Simulink and the electromagnetic transient program (EMTP-ATP) are presented. The validity and effectiveness of the devised control algorithms are validated by the simulation results.

**Streszczenie.** Zaprezentowano modelowanie i projekt trzyfazowego kaskadowego wielopoziomowego filtra aktywnego mocy. Opracowano predykcyjny sterownik prądu z algorytmem bazującym na obserwatorze Leuenbergera. Zaprezentowano symulacje z wykorzystaniem programu Matlab/Simulink i EMTP-ATP. (Projekt sterownika do trzyfazowego kaskadowego wielopoziomowego filtra aktywnego mocy)

**Keywords:** Power quality, Harmonic pollution, Active power filter, Cascaded H-bridge, Robust predictive current controller  
**Słowa kluczowe:** jakość energii, fiiltr aktywny, sterownik prądu

## I. Introduction

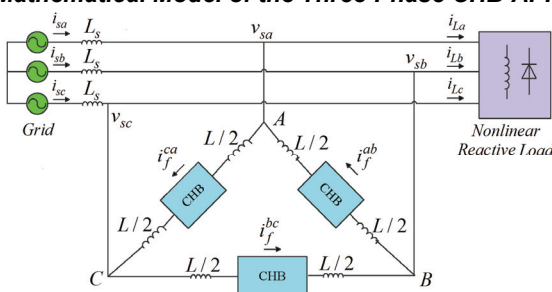
Due to the proliferation of nonlinear loads, the harmonic pollution of the electric power system is increasing rapidly. These nonlinear loads draw a large amount of distorted currents from the utility, results in significant power quality contamination and severe electromagnetic interference to the sensitive loads [1]. The active power filters (APFs) are considered as the most effective solution to the harmonic pollution problems due to the advancement of the modern control theory, digital signal processing techniques and the power semiconductor devices [2-5].

Among various topologies of the APFs, the cascaded H-bridge multilevel configuration is appreciated for the high-power medium-voltage applications due to its modularity and flexibility of manufacturing. However, restricted by the limited switching frequency of the power devices, achieving stable operation and accurate reference tracking is rather complicated. This paper aims to present the mathematical model and predictive current controller design for the CHB-APF, which can be applied to practical applications [6-10].

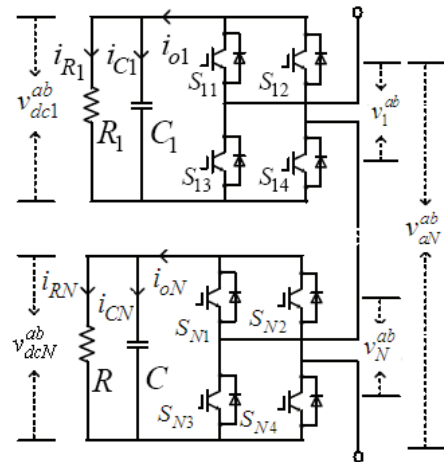
The organization of this paper is as follows. Section II presents the modelling and controller design for the three phase cascaded H-bridge active power filter (APF), and the Luenberger observer is devised to enhance the steady state precision and dynamic characteristics of the current controller with enhanced robustness under control delay and parameter variations. Sections III and IV present the simulation results obtained from Matlab/Simulink and the electromagnetic transient program (EMTP-ATP) to validate the effectiveness of the control algorithm. Finally, Section V concludes this paper.

## II. Modelling and Controller Design for the Three-Phase Cascaded H-bridge (CHB) Active Power Filter (APF)

### A. Mathematical Model of the Three-Phase CHB-APF



(a) Overview of the proposed three-phase CHB-APF.



(b) Circuit diagram of the chain-link between phases 'A' and 'B'.  
Fig. 1. The schematic of the three-phase cascaded H-bridge (CHB) multilevel active power filter (CHB-APF).

Fig.1 shows the circuit configuration of the three-phase cascaded H-bridge multilevel active power filter (APF). Fig.1(a) shows the overview of the CHB-APF, where the multilevel inverter chain is connected in delta-connection. Fig.1(b) denotes the detailed illustration of the chain-link between the phase 'A' and 'B' [2, 6, 11].

In Fig.1, the grid voltages are denoted as  $v_{sa}$ ,  $v_{sb}$ ,  $v_{sc}$ , the phase to phase voltages are represented as  $v_{ab}$ ,  $v_{bc}$  and  $v_{ca}$ , and the multilevel inverter output voltages are denoted as  $v_{aN}^{ab}$ ,  $v_{aN}^{bc}$ ,  $v_{aN}^{ca}$ . The injection currents of the cascaded inverters are denoted as  $i_f^{ab}$ ,  $i_f^{bc}$  and  $i_f^{ca}$ . The differential equations of the CHB-APF can be derived as [11-13]:

$$(1) \quad \begin{cases} \frac{d}{dt} i_f^{ab} = -\frac{r_L}{L} \cdot i_f^{ab} + \frac{1}{L} (v_{aN}^{ab} - v_{ab}) \\ \frac{d}{dt} i_f^{bc} = -\frac{r_L}{L} \cdot i_f^{bc} + \frac{1}{L} (v_{aN}^{bc} - v_{bc}) \\ \frac{d}{dt} i_f^{ca} = -\frac{r_L}{L} \cdot i_f^{ca} + \frac{1}{L} (v_{aN}^{ca} - v_{ca}) \end{cases}$$

To simplify theoretical derivations of the mathematical model for the three-phase multilevel CHB-APF, Eq.(1) can be rewritten as:

$$(2) \quad \frac{d}{dt} \mathbf{i}_f^{abc} = -\frac{r_L}{L} \cdot \mathbf{i}_f^{abc} + \frac{1}{L} \mathbf{v}^{abc}$$

where  $\mathbf{i}_f^{abc} = [i_f^{ab}, i_f^{bc}, i_f^{ca}]^T$ ,  $\mathbf{v}^{abc} = \mathbf{v}_{aN}^{abc} - \mathbf{v}_s^{abc}$ , and the voltage vectors  $\mathbf{v}_{aN}^{abc}$  and  $\mathbf{v}_s^{abc}$  are denoted as:

$$(3) \quad \mathbf{v}_{aN}^{abc} = \frac{1}{L} [\mathbf{v}_{aN}^{ab}, \mathbf{v}_{aN}^{bc}, \mathbf{v}_{aN}^{ca}]^T, \mathbf{v}_s^{abc} = \frac{1}{L} [\mathbf{v}_{sab}, \mathbf{v}_{sbc}, \mathbf{v}_{sca}]^T$$

The three-phase currents and voltages are transformed into the synchronous reference frame (SRF) [2, 6, 8, 11], hence the following equations can be derived:

$$(4) \quad \mathbf{i}_f^{dq} \equiv [i_d, i_q]^T = T_{abc2dq} \cdot \mathbf{i}_f^{abc}, \mathbf{v}_f^{dq} \equiv [v_d, v_q]^T = T_{abc2dq} \cdot \mathbf{v}^{abc}$$

In the synchronous  $d$ - $q$  frame, Eq.(1) can be written as:

$$(5) \quad \frac{d}{dt} \mathbf{i}_f^{dq} = \mathbf{A} \cdot \mathbf{i}_f^{dq} + \mathbf{B} \cdot \mathbf{v}_f^{dq}$$

where  $\mathbf{v}^{dq} = \mathbf{v}_{aN}^{dq} - \mathbf{v}_s^{dq}$ ,  $\mathbf{v}_{aN}^{dq} = [v_{aN}^d, v_{aN}^q]^T$ ,  $\mathbf{v}_s^{dq} = [v_s^d, v_s^q]^T$ , and the state matrices  $\mathbf{A}$  and  $\mathbf{B}$  can be written as:

$$(6) \quad \mathbf{A} = \begin{bmatrix} -\frac{r_L}{L} & \omega_0 \\ -\omega_0 & -\frac{r_L}{L} \end{bmatrix}, \mathbf{B} = \frac{1}{L} \cdot \mathbf{I}_{2 \times 2}$$

where  $\omega_0$  denotes the grid frequency, the state transition matrix of Eq.(5) is represented as:

$$(7) \quad \Phi(t) = e^{\mathbf{A}t}$$

In order to derive the eigenvalue of the state matrix  $\mathbf{A}$ , the eigen equation is first checked in the following equation:

$$(8) \quad |\lambda \mathbf{I} - \mathbf{A}| = \begin{vmatrix} \lambda + r_L/L & -\omega_0 \\ \omega_0 & \lambda + r_L/L \end{vmatrix} = \lambda^2 + \frac{2r_L}{L}\lambda + \frac{r_L^2}{L^2} + \omega_0^2 = 0$$

From Eq.(8), the eigen values are derived as  $\lambda = -r_L/L \pm j\omega_0$ . Followed by the principle of linear algebra, there exists a non-singular transformation matrix  $\mathbf{P}$ , by which the matrix  $\mathbf{A}$  can be transformed into a diagonal matrix as in Eq.(9).

$$(9) \quad \mathbf{A} = \mathbf{P}^{-1} \mathbf{A} \mathbf{P} = \begin{bmatrix} -r_L/L + j\omega_0 & 0 \\ 0 & -r_L/L - j\omega_0 \end{bmatrix}$$

where the transforming matrices  $\mathbf{P}$  and  $\mathbf{P}^{-1}$  are denoted as:

$$(10) \quad \mathbf{P} = \begin{bmatrix} 1 & 1 \\ j & -j \end{bmatrix}, \mathbf{P}^{-1} = \frac{1}{2} \begin{bmatrix} 1 & -j \\ 1 & j \end{bmatrix}$$

Therefore, the exponential function  $e^{\mathbf{A}t}$  is derived as:

$$(11) \quad e^{\mathbf{A}t} = \mathbf{P} \cdot e^{\mathbf{A}t} \cdot \mathbf{P}^{-1} = e^{-\frac{r_L}{L}t} \cdot \begin{bmatrix} \cos(\omega_0 t) & \sin(\omega_0 t) \\ -\sin(\omega_0 t) & \cos(\omega_0 t) \end{bmatrix}$$

Assuming the sampling time is  $T_s$ , hence the differential equation Eq.(5) can be discretized as:

$$(12) \quad \mathbf{i}_f^{dq}(k+1) = \mathbf{A}_{dis} \cdot \mathbf{i}_f^{dq}(k) + \mathbf{B}_{dis} \cdot \mathbf{v}_f^{dq}(k)$$

where the matrices  $\mathbf{A}_{dis}$  and  $\mathbf{B}_{dis}$  are derived as:

$$(13) \quad \mathbf{A}_{dis} = \Phi(T_s) = e^{-\frac{r_L}{L}T_s} \cdot \begin{bmatrix} \cos(\omega_0 T_s) & \sin(\omega_0 T_s) \\ -\sin(\omega_0 T_s) & \cos(\omega_0 T_s) \end{bmatrix}$$

$$(14) \quad \mathbf{B}_{dis} = \mathbf{A}^{-1}(\mathbf{A}_{dis} - \mathbf{I})\mathbf{B}$$

Since the sampling time  $T_s$  is much smaller than the period of fundamental grid voltage, hence  $\omega_0 T_s \ll 1$  holds, thus  $\cos(\omega_0 T_s) \approx 1$ ,  $\sin(\omega_0 T_s) \approx \omega_0 T_s$ . Moreover, the following approximation holds for the exponential function.

$$(15) \quad e^{-\frac{r_L}{L}T_s} = 1 - \frac{r_L}{L}T_s + \frac{1}{2!}(\frac{r_L}{L})^2 T_s^2 - \frac{1}{3!}(\frac{r_L}{L})^3 T_s^3 + \frac{1}{4!}(\frac{r_L}{L})^4 T_s^4 + \dots$$

Substituting Eq.(15) back into Eq.(12), the discrete state matrix  $\mathbf{A}_{dis}$  can be derived as:

$$(16) \quad \mathbf{A}_{dis} = \Phi(T_s) \approx \begin{bmatrix} 1 - \frac{r_L}{L}T_s & \omega_0 T_s \\ -\omega_0 T_s & 1 - \frac{r_L}{L}T_s \end{bmatrix}$$

Besides, the inverse matrix of the matrix  $\mathbf{A}$  is derived as:

$$(17) \quad \mathbf{A}^{-1} = \mathbf{P} \mathbf{A}^{-1} \mathbf{P}^{-1} = \frac{1}{(\frac{r_L}{L})^2 + \omega_0^2} \begin{bmatrix} -\frac{r_L}{L} & -\omega_0 \\ \omega_0 & -\frac{r_L}{L} \end{bmatrix}$$

Substituting Eqs.(15)-(16) back into Eq.(13), the discrete representation of the matrix  $\mathbf{B}$  can be derived as:

$$(18) \quad \mathbf{B}_{dis} = \frac{1/L}{(\frac{r_L}{L})^2 + \omega_0^2} \begin{bmatrix} -\frac{r_L}{L} & -\omega_0 \\ \omega_0 & -\frac{r_L}{L} \end{bmatrix} \cdot \begin{bmatrix} -\frac{r_L}{L}T_s & \omega_0 T_s \\ -\omega_0 T_s & -\frac{r_L}{L}T_s \end{bmatrix} \cdot \mathbf{I}_{2 \times 2} = \frac{1/L}{(\frac{r_L}{L})^2 + \omega_0^2} \begin{bmatrix} (\frac{r_L}{L})^2 T_s + \omega_0^2 T_s & 0 \\ 0 & (\frac{r_L}{L})^2 T_s + \omega_0^2 T_s \end{bmatrix} \cdot \mathbf{I}_{2 \times 2} = \frac{T_s}{L} \mathbf{I}_{2 \times 2}$$

## B. Robust Current Controller Design for the CHB-APP based on the Luenberger Observer

Fig.2 shows the relations between the sampling time and the instantaneous tracking current with respect to the PWM modulation signal and the carrier signal. The PWM carrier is a triangular waveform, and the period of the carrier and sampling interval are identical to  $T_s$ . The PWM modulation signal is represented by the dashed line, and the present calculation interval lies between the instants  $(k-1)T_s \sim kT_s$ . In the practical applications, the sampling time lies within the present control cycle or within the previous control cycle, as denoted by the points 'B' and 'A' in Fig.2.

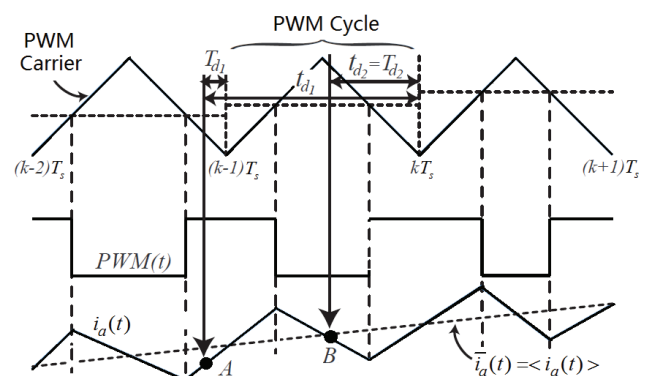


Fig.2 The relations between the sampling instants and output current with respect to the modulation signal and the PWM output.

Therefore, the equivalent control delays can be denoted as  $t_{d2}=T_{d2}$ ,  $t_{d1}=T_{d1}+T_s$ . The model of the current controller would be derived in the forthcoming section with the effect of control delay included [14, 15].

Defining  $\mathbf{i}_{f,d}^{dq}(t) \equiv \mathbf{i}_f^{dq}(t-t_d)$ ,  $\mathbf{v}_{s,d}^{dq}(t) \equiv \mathbf{v}_s^{dq}(t-t_d)$ , thus Eq.(5) can be discretized as:

$$(19) \quad \mathbf{i}_{f,d}^{dq}(t) \equiv \mathbf{i}_f^{dq}(t-t_d) = e^{\mathbf{A}(t-t_d-t_0)} \cdot \mathbf{i}_f^{dq}(t_0) + \int_{t_0}^{t-d} e^{\mathbf{A}(t-t_d-\tau)} \cdot \mathbf{B} \cdot \mathbf{v}_f^{dq}(\tau) d\tau$$

Let  $t_0=kT_s-t_d$ ,  $t=(k+1)T_s$ , thus Eq.(19) can be rewritten as:

$$(20) \quad \begin{aligned} \mathbf{i}_{f,d}^{dq}(k+1) &= \mathbf{A}_{dis} \cdot \mathbf{i}_{f,d}^{dq}(k) \\ &+ \int_{kT_s-t_d}^{(k+1)T_s-t_d} e^{\mathbf{A}((k+1)T_s-t_d-\tau)} \cdot \mathbf{B} \cdot [\mathbf{v}_{aN}^{dq}(\tau) - \mathbf{v}_s^{dq}(\tau)] d\tau \end{aligned}$$

In the synchronous reference frame (SRF),  $\mathbf{v}_s^{dq}(k)$  is almost constant, hence the following approximation holds.

$$(21) \quad \int_{kT_s-t_d}^{(k+1)T_s-t_d} e^{\mathbf{A}((k+1)T_s-t_d-\tau)} \cdot \mathbf{B} \cdot \mathbf{v}_s^{dq}(\tau) d\tau \approx \mathbf{B}_{dis} \cdot \tilde{\mathbf{v}}_{s,d}^{dq}(k)$$

Defining control delay  $t_d=T_d+mT_s$ , where  $m=\{0, 1\}$  and  $T_d < T_s$  holds, and assuming  $\mathbf{v}_{aN}^{dq}(t)$  is constant during two sampling points, thus the following equation holds.

$$(22) \quad \begin{aligned} &\int_{kT_s-t_d}^{(k+1)T_s-t_d} e^{\mathbf{A}((k+1)T_s-t_d-\tau)} \cdot \mathbf{B} \cdot \mathbf{v}_{aN}^{dq}(\tau) d\tau \\ &= \int_{(k-m)T_s-T_d}^{(k-m)T_s-T_d} e^{\mathbf{A}((k+1)T_s-t_d-\tau)} \cdot \mathbf{B} \cdot \mathbf{v}_{aN}^{dq}(\tau) d\tau \\ &+ \int_{(k-m)T_s}^{(k-m+1)T_s-T_d} e^{\mathbf{A}((k+1)T_s-t_d-\tau)} \cdot \mathbf{B} \cdot \mathbf{v}_{aN}^{dq}(\tau) d\tau \\ &= \mathbf{B}_{dis}^{(0)} \cdot \mathbf{v}_{aN}^{dq}(k-m) + \mathbf{B}_{dis}^{(1)} \cdot \mathbf{v}_{aN}^{dq}(k-m-1) \end{aligned}$$

where the matrices  $\mathbf{B}_{dis}^{(0)}$  and  $\mathbf{B}_{dis}^{(1)}$  can be derived as:

$$(23) \quad \begin{aligned} \mathbf{B}_{dis}^{(0)} &= \mathbf{A}^{-1} \cdot [\Phi(T_s - T_d) - \mathbf{I}] \cdot \mathbf{B}, \\ \mathbf{B}_{dis}^{(1)} &= \mathbf{A}^{-1} \cdot [\mathbf{A}_{dis} - \Phi(T_s - T_d)] \cdot \mathbf{B} = \mathbf{B}_{dis} - \mathbf{B}_{dis}^{(0)} \end{aligned}$$

Substituting Eqs.(20) and (21) back into Eq.(19), we get:

$$(24) \quad \begin{aligned} \mathbf{i}_{f,d}^{dq}(k+1) &= \mathbf{A}_{dis} \cdot \mathbf{i}_{f,d}^{dq}(k) - \mathbf{B}_{dis} \cdot \tilde{\mathbf{v}}_{s,d}^{dq}(k) \\ &+ \mathbf{B}_{dis}^{(0)} \cdot \mathbf{v}_{aN}^{dq}(k-m) + \mathbf{B}_{dis}^{(1)} \cdot \mathbf{v}_{aN}^{dq}(k-m-1) \end{aligned}$$

When  $m=1$  and  $T_d \approx 0$ , Eq.(24) can be rewritten as:

$$(25) \quad \mathbf{i}_{f,d}^{dq}(k+1) = \mathbf{A}_{dis} \cdot \mathbf{i}_{f,d}^{dq}(k) + \mathbf{B}_{dis} \cdot [\mathbf{v}_{aN}^{dq}(k-1) - \tilde{\mathbf{v}}_{s,d}^{dq}(k)]$$

From Eq.(25), the output voltages of the cascaded inverter in the  $d-q$  reference frame can be derived as:

$$(26) \quad \mathbf{v}_{aN}^{dq}(k) = \mathbf{B}_{dis,m}^{-1} \cdot [\mathbf{i}_{f,d}^{dq}(k+2) - \mathbf{A}_{dis,m} \cdot \mathbf{i}_{f,d}^{dq}(k+1)] + \tilde{\mathbf{v}}_{s,d}^{dq}(k+1)$$

where the matrices  $\mathbf{A}_{dis,m}$  and  $\mathbf{B}_{dis,m}$  can be derived as:

$$(27) \quad \begin{aligned} \mathbf{A}_{dis,m} &= \mathbf{A}_{dis} \Big|_{L=L_m} = \begin{bmatrix} 1 - \frac{r_L}{L_m} T_s & \omega_0 T_s \\ -\omega_0 T_s & 1 - \frac{r_L}{L_m} T_s \end{bmatrix} \\ \mathbf{B}_{dis,m} &= \mathbf{B}_{dis} \Big|_{L=L_m} = \frac{T_s}{L_m} \mathbf{I} \end{aligned}$$

Let  $\mathbf{i}_{f,d}^{dq}(k+2) = \mathbf{i}_{ref}^{dq}(k)$ , the predictive current control law based on the two-point deadbeat scheme is derived as:

$$(28) \quad \mathbf{v}_{aN}^{dq}(k) = \mathbf{B}_{dis,m}^{-1} \cdot [\mathbf{i}_{ref}^{dq}(k) - \mathbf{A}_{dis,m} \cdot \mathbf{i}_{f,d}^{dq}(k+1)] + \tilde{\mathbf{v}}_{s,d}^{dq}(k+1)$$

From Eq.(28), it can be deduced that, to calculate the term  $\mathbf{v}_{aN}^{dq}(k)$ , the variables  $\mathbf{i}_{f,d}^{dq}(k+1)$  and  $\tilde{\mathbf{v}}_{s,d}^{dq}(k+1)$  needs to be estimated. In this paper, the Luenberger observer is used to estimate the currents in  $d-q$  reference frame, the equation can be denoted as:

$$(29) \quad \begin{aligned} \hat{\mathbf{i}}_{f,d}^{dq}(k+1) &= (\mathbf{A}_{dis,m} - \mathbf{M}_{dis}) \cdot \hat{\mathbf{i}}_{f,d}^{dq}(k) + \mathbf{M}_{dis} \cdot \mathbf{i}_{f,d}^{dq}(k) \\ &+ \mathbf{B}_{dis,m} \cdot [\mathbf{v}_{aN}^{dq}(k-1) - \tilde{\mathbf{v}}_{s,d}^{dq}(k)] \end{aligned}$$

where  $\hat{\mathbf{i}}_{f,d}^{dq}(k)$  is an estimate of  $\mathbf{i}_{f,d}^{dq}(k)$ ,  $\mathbf{M}_{dis}$  denotes the gain matrix of the Luenberger observer. When  $\mathbf{A}_{dis,m} \rightarrow \mathbf{M}_{dis}$ , the Luenberger-based predictive algorithm reduces to the traditional predictive current control algorithm. Notably, the parameter of the matrix  $\mathbf{M}_{dis}$  must satisfy the condition that the eigenvalues of  $|\mathbf{A}_{dis,m} - \mathbf{M}_{dis}|$  are within the unit circle. As for the estimation of  $\tilde{\mathbf{v}}_{s,d}^{dq}(k+1)$ , the interpolation is utilized:

$$(30) \quad \tilde{\mathbf{v}}_{s,d}^{dq}(k+1) \approx 2\mathbf{v}_{s,d}^{dq}(k) - \mathbf{v}_{s,d}^{dq}(k-1)$$

From Eqs.(24)-(29), the block diagrams of Luenberger observer-based robust predictive current controller can be derived, as shown in Fig.3.

Fig.3(a) shows the detailed block diagram and Fig.3(b) and (c) show the simplified block diagram. The predictive current controller is simplified in a step-by-step manner in order to better illustrate the equivalent transfer functions of the current controllers in the following subsections. Based on the principle of the automatic control theory, the prefilter  $\mathbf{G}_{ff}(z)$  can be devised as:

$$(31) \quad \mathbf{G}_{ff}(z) = \mathbf{A}_{dis,m}^{-1} \cdot [\mathbf{I} - z^{-1} \cdot (\mathbf{A}_{dis,m} - \mathbf{M}_{dis})] \cdot \mathbf{M}_{dis}^{-1}$$

And the controller  $\mathbf{G}_{c1}(z)$  and  $\mathbf{G}_{c2}(z)$  can be denoted as:

$$(32) \quad \mathbf{G}_{c1}(z) = \mathbf{G}_{ff}^{-1}(z) = \mathbf{M}_{dis} \cdot [\mathbf{I} - z^{-1} \cdot (\mathbf{A}_{dis,m} - \mathbf{M}_{dis})]^{-1} \cdot \mathbf{A}_{dis,m}$$

$$(33) \quad \mathbf{G}_{c2}(z) = \frac{\mathbf{B}_{dis,m}^{-1} \cdot [\mathbf{I} - (\mathbf{A}_{dis,m} - \mathbf{M}_{dis}) \cdot z^{-1}]}{\mathbf{I} + \mathbf{M}_{dis} \cdot z^{-1}}$$

Therefore, the transfer function of the current controller  $\mathbf{G}_c(z)$  can be derived as:

$$(34) \quad \begin{aligned} \mathbf{G}_c(z) &= \mathbf{G}_{c1}(z) \cdot \mathbf{G}_{c2}(z) \\ &= \mathbf{A}_{dis,m} \cdot \mathbf{B}_{dis,m}^{-1} \cdot (\mathbf{z} \cdot \mathbf{I} + \mathbf{M}_{dis})^{-1} \cdot \mathbf{M}_{dis} \cdot \mathbf{z} \end{aligned}$$

The open-loop transfer function  $\mathbf{H}_{open}(z)$  is derived as:

$$(35) \quad \mathbf{H}_{open}(z) = (z \cdot \mathbf{I} - \mathbf{A}_{dis})^{-1} \mathbf{B}_{dis} \mathbf{B}_{dis,m}^{-1} \mathbf{A}_{dis,m} (z \cdot \mathbf{I} + \mathbf{M}_{dis})^{-1} \mathbf{M}_{dis}$$

When  $L \approx L_m$ , the matrices  $\mathbf{A}_{dis} \approx \mathbf{A}_{dis,m}$ ,  $\mathbf{B}_{dis} \approx \mathbf{B}_{dis,m}$ , hence Eq.(34) can be represented as:

$$(36) \quad \mathbf{H}_{open}(z) = (z \cdot \mathbf{I} - \mathbf{A}_{dis,m})^{-1} \cdot \mathbf{A}_{dis,m} \cdot (z \cdot \mathbf{I} + \mathbf{M}_{dis})^{-1} \cdot \mathbf{M}_{dis}$$

Hence, the closed-loop transfer function of the current loop including the prefilter  $\mathbf{G}_{ff}(z)$  can be derived as:

$$(37) \quad \begin{aligned} \mathbf{G}_{close}(z) &= \mathbf{H}_{open}(z) \cdot [\mathbf{I} + \mathbf{H}_{open}(z)]^{-1} \cdot \mathbf{G}_{ff}(z) \\ &= \{\mathbf{G}_{ff}^{-1}(z) [\mathbf{I} + \mathbf{H}_{open}^{-1}(z)]\}^{-1} \end{aligned}$$

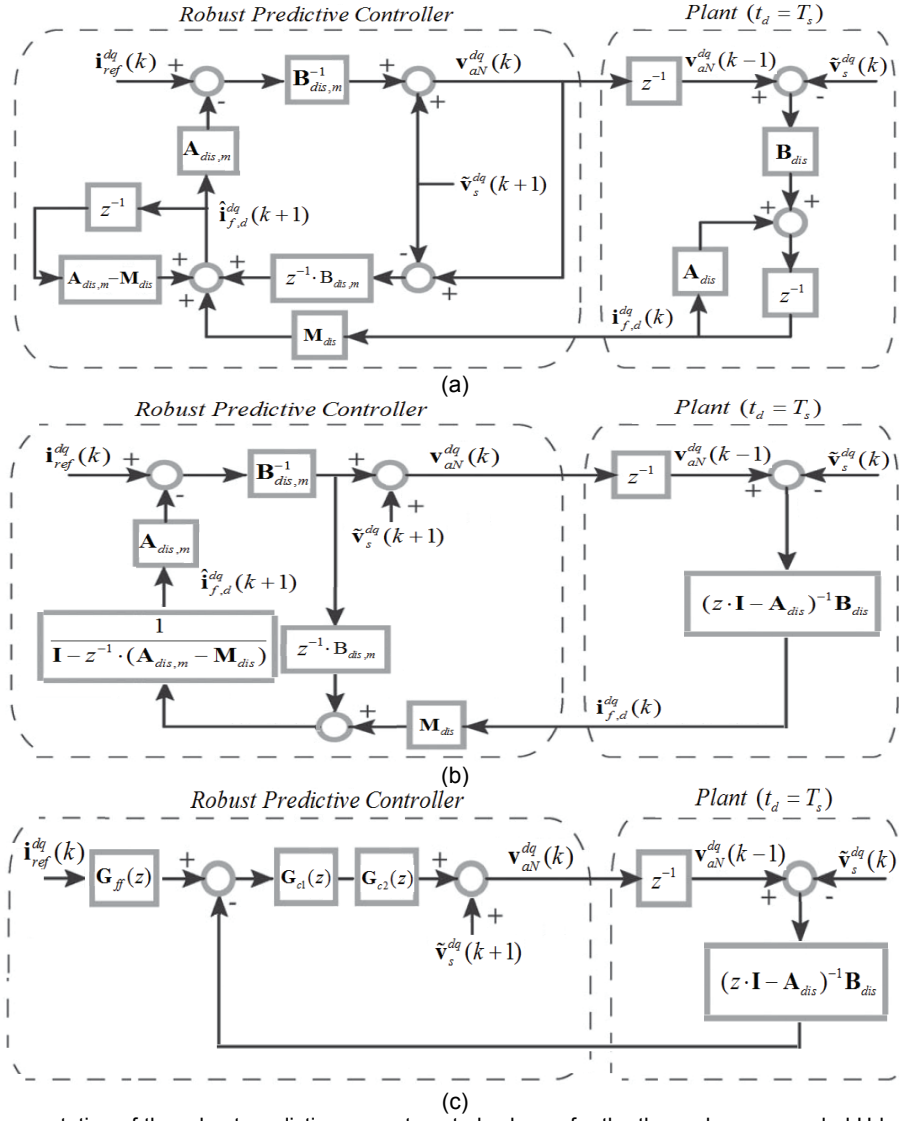


Fig.3 The discrete representation of the robust predictive current control scheme for the three-phase cascaded H-bridge active power filter (CHB-APF) based on the Luenberger observer. (a) The detailed control block diagram, (b), (c) The simplified control block diagram.

Applying the inverse operation to both sides of Eq.(35), thus the inverse matrix of  $\mathbf{H}_{open}(z)$  can be derived as:

$$(38) \quad \begin{aligned} \mathbf{H}_{open}^{-1}(z) &= (z \cdot \mathbf{A}_{dis,m}^{-1} - \mathbf{I})(z \cdot \mathbf{M}_{dis}^{-1} + \mathbf{I}) \\ &= z^2 \cdot \mathbf{A}_{dis,m}^{-1} \cdot \mathbf{M}_{dis}^{-1} + z \cdot \mathbf{I} \cdot (\mathbf{A}_{dis,m}^{-1} - \mathbf{M}_{dis}^{-1}) - \mathbf{I} \end{aligned}$$

Therefore, the transfer function  $\mathbf{I} + \mathbf{H}_{open}^{-1}(z)$  is derived as:

$$(39) \quad \begin{aligned} \mathbf{I} + \mathbf{H}_{open}^{-1}(z) &= z^2 \cdot \mathbf{A}_{dis,m}^{-1} \cdot \mathbf{M}_{dis}^{-1} + z \cdot \mathbf{I} \cdot (\mathbf{A}_{dis,m}^{-1} - \mathbf{M}_{dis}^{-1}) \\ &= z^2 \cdot \mathbf{A}_{dis,m}^{-1} \cdot \mathbf{M}_{dis}^{-1} \cdot [\mathbf{I} + z^{-1} \cdot (\mathbf{M}_{dis} - \mathbf{A}_{dis,m})] = z^2 \cdot \mathbf{G}_{ff}(z) \end{aligned}$$

From Eq.(36) and Eq.(38), we get:

$$(40) \quad \mathbf{G}_{close}(z) = \{\mathbf{G}_{ff}^{-1}(z) \cdot z^2 \cdot \mathbf{G}_{ff}(z)\}^{-1} = z^{-2}.$$

From Eq.(39), it can be deduced that the Luenberger observer-based robust predictive current controller can be equivalent to the two-step deadbeat controller if the gain matrix  $\mathbf{M}_{dis}$  and the inverse matrix  $\mathbf{G}_{ff}^{-1}(z)$  are stable.

To simplify the analysis, Eq.(23) is approximated as:

$$(41) \quad \begin{aligned} \mathbf{B}_{dis}^{(0)} &= \mathbf{A}^{-1} \cdot [\Phi(T_s - T_d) - \mathbf{I}] \cdot \mathbf{B} \\ &= \frac{(T_s - T_d)}{L} \mathbf{I}_{2 \times 2}, \mathbf{B}_{dis}^{(1)} = \mathbf{B}_{dis} - \mathbf{B}_{dis}^{(0)} = \frac{T_d}{L} \mathbf{I}_{2 \times 2} \end{aligned}$$

When the sampling interval  $T_s$  is sufficiently small, the matrices  $\mathbf{A}_{dis}$  and  $\mathbf{A}_{dis,m}$  can be simplified to the diagonal matrices, i.e.,  $\mathbf{A}_{dis} \approx \mathbf{A}_{dis,m} \approx e^{(-r_L/L)T_s} \cdot \mathbf{I}$ . Hence, Eq.(20) can be rewritten as:

$$(42) \quad \begin{aligned} \hat{\mathbf{i}}_{f,d}^{dq}(k+1) &\approx e^{(-r_L/L)T_s} \cdot \hat{\mathbf{i}}_{f,d}^{dq}(k) + \frac{T_s}{L} [(1-\delta) \cdot \mathbf{v}_{aN}^{dq}(k-m) \\ &\quad + \delta \cdot \mathbf{v}_{aN}^{dq}(k-m-1) - \tilde{\mathbf{v}}_{s,d}^{dq}(k)] \end{aligned}$$

where  $\delta = T_d/T_s$ . In this study, the gain matrix of Luenberger observer is designed as diagonal matrix, i.e.,  $\mathbf{M}_{dis} = \xi_0 \mathbf{I}$  and the coefficient  $\xi_0 \in [0, 1]$  should be satisfied.

### C. Performance Evaluation of Current Controller under Different Control Delay and Parameter Variations

The proposed current controller is a typical multi-input multi-output (MIMO) system, which can be decoupled into two independent single-input single-output (SISO) systems, thus the decoupling between the  $d$ -axis and  $q$ -axis can be ensured [8, 9, 12-14].

Figs.4-8 show the step response and impulse response of the Luenberger observer-based robust predictive current controller under different control delay when the parameters  $L_m=L$  and  $T_s=100\mu s$ . In these figures, the step and impulse responses from the  $d$ - $q$  axis references to the actual  $d$ - $q$

axis currents are plotted, and the parameters  $m$ ,  $\delta$  assumes the following four values:  $\{m=1, \delta=0\}$ ,  $\{m=1, \delta=0.2\}$ ,  $\{m=1, \delta=0.5\}$ ,  $\{m=0, \delta=0.5\}$ .

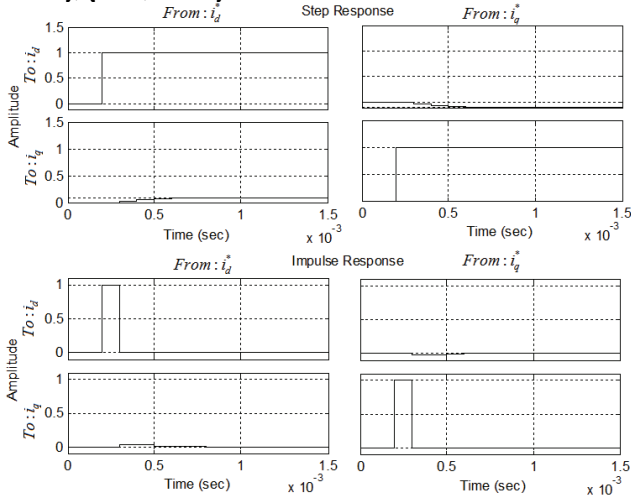


Fig.4 The step response and impulse response from the reference  $i_d^*$ ,  $i_a^*$  to  $i_d$ ,  $i_a$  when  $L_m=L$ ,  $m=1$ ,  $\delta=0$ .

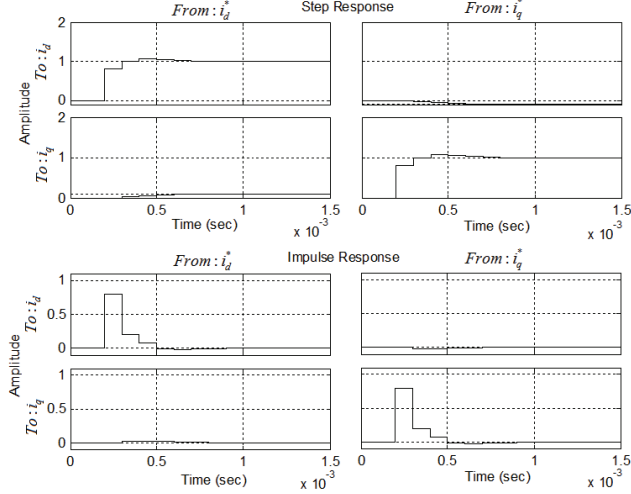


Fig.5 The step response and impulse response from the reference  $i_d^*$ ,  $i_q^*$  to  $i_d$ ,  $i_q$  when  $L_m=L$ ,  $m=1$ ,  $\delta=0.2$ .

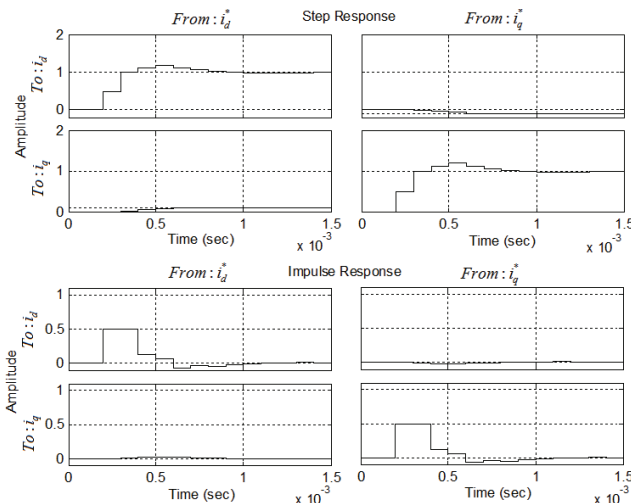


Fig.6 The step response and impulse response from the reference  $i_d^*$ ,  $i_q^*$  to  $i_d$ ,  $i_q$  when  $L_m=L$ ,  $m=1$ ,  $\delta=0.5$ .

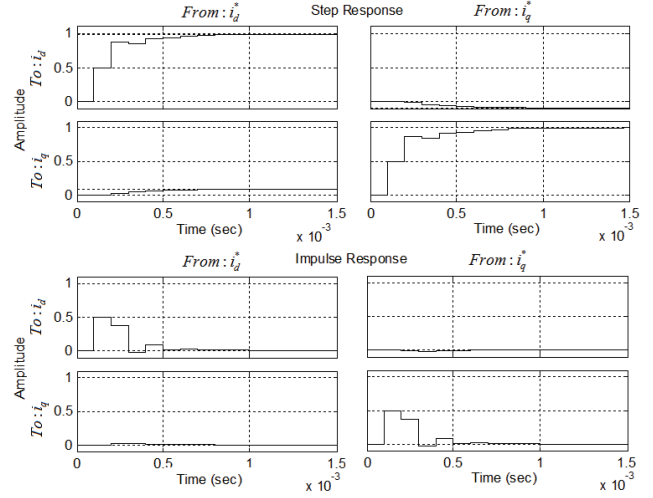


Fig.7 The step response and impulse response from the reference  $i_d^*$ ,  $i_q^*$  to  $i_d$ ,  $i_q$  when  $L_m=L$ ,  $m=0$ ,  $\delta=0.5$ .

It can be observed from Fig.4 that, when  $m=1$  and  $\delta=0$ , the response time of  $d$ -axis and  $q$ -axis current controllers are identical to  $200\mu s$ , which is exactly two beat lagging the reference signal. From Fig.5, it can be observed that, when  $m=1$ ,  $\delta=0.2$ , the response time of  $d$ -axis and  $q$ -axis current controllers are identical to  $700\mu s$ . Fig.6 shows that, when  $m=1$ ,  $\delta=0.5$ , the response time of  $d$ -axis and  $q$ -axis current controllers are identical to  $800\mu s$ . Fig.7 shows that, when  $m=0$ ,  $\delta=0.5$ , the response time of  $d$ -axis and  $q$ -axis current controllers are identical to  $600\mu s$ . And the transient overshoots are within  $0.05pu$  in Figs.5-7. Notably, it can be observed from Figs.4-7 that the step response and impulse response from the  $d$ -axis (or  $q$ -axis) reference to the  $q$ -axis ( $d$ -axis) current have no significant effect. Hence, it can be deduced that the decoupling between the  $d$ -axis and  $q$ -axis is achieved by selecting the gain matrix as diagonal matrix in the Luenberger observer.

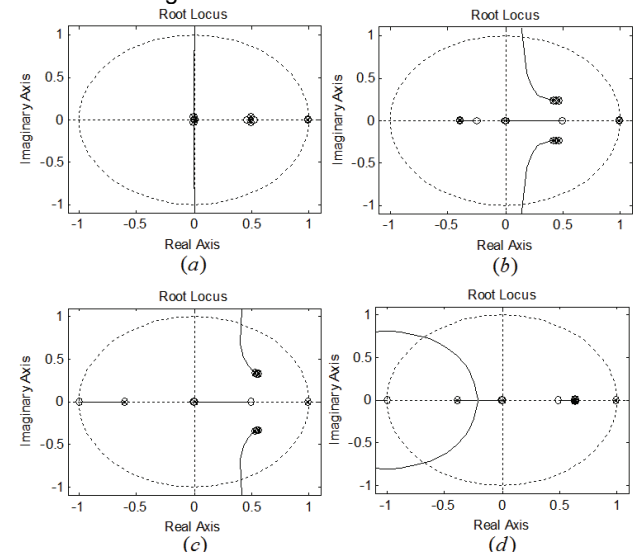


Fig.8 The root locus diagram of the proposed robust predictive controller based on the Luenberger observer, the  $d$ -axis controller (a)  $m=1$ ,  $\delta=0$ ; (b)  $m=1$ ,  $\delta=0.2$ ; (c)  $m=1$ ,  $\delta=0.5$ ; (d)  $m=0$ ,  $\delta=0.5$ .

Fig.8 shows the root locus plot of the  $d$ -axis controller of the proposed robust predictive control algorithm based on the Luenberger observer when  $L_m=L$ ,  $T_s=100\mu s$ , and the parameters  $m$ ,  $\delta$  are selected as:  $\{m=1, \delta=0\}$ ,  $\{m=1, \delta=0.2\}$ ,  $\{m=1, \delta=0.5\}$ ,  $\{m=0, \delta=0.5\}$ . Fig.9 shows the root locus plot of the cross-coupling term in the current controller based on the Luenberger observer when  $L_m=L$ ,  $T_s=100\mu s$ , and the parameters  $m$ ,  $\delta$  are same as those in Fig.8.

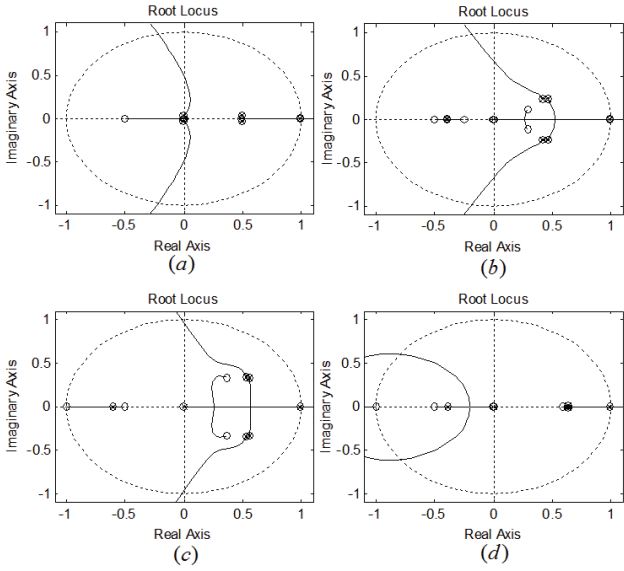


Fig.9 The root locus diagram of the proposed robust predictive controller based on the Luenberger observer, the cross coupling term (a)  $m=1$ ,  $\delta=0$ ; (b)  $m=1$ ,  $\delta=0.2$ ; (c)  $m=1$ ,  $\delta=0.5$ ; (d)  $m=0$ ,  $\delta=0.5$ .

It can be observed from Fig.8 and Fig.9 that, the closed-loop poles are located within the unit circle, and the zero at  $z=1$  cancels the unstable pole  $p=1$ , thus the Luenberger observer ensures closed-loop stability of the current loop controller under a large control delay. On the other hand, the intersection of the root locus with the unit circle is affected by the effective control delay. When the parameters  $m=0$ ,  $\delta=0.5$ , the intersection locates at the left half plane of the unit circle with the maximum bandwidth and the cutoff frequency. With the increase of the control delay, the trajectory of intersection point moves to the right half plane of the unit circle gradually, thus the closed-loop bandwidth would reduce and the cutoff frequency is also diminished.

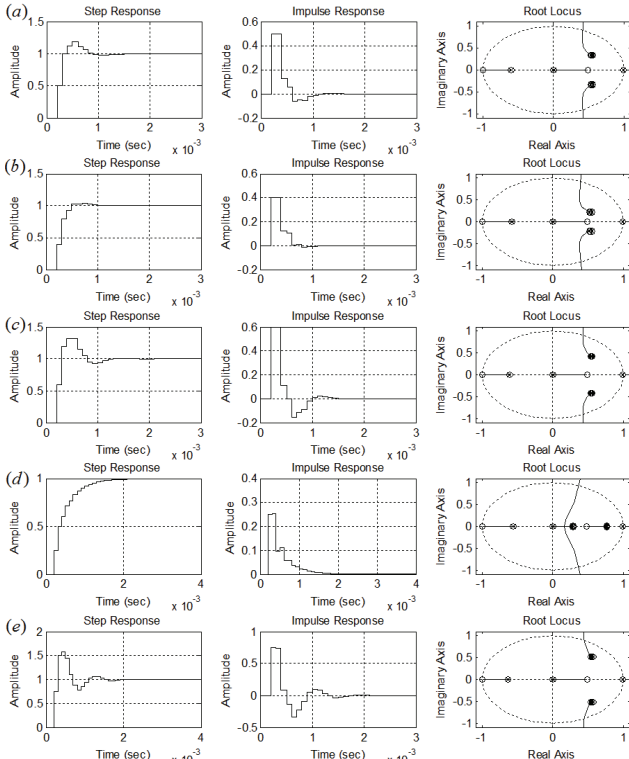


Fig.10 The robustness analysis of the proposed predictive current controller based on the Luenberger observer when  $m=1$ ,  $\delta=0.5$ . (a)  $L_m=L$ ; (b)  $L_m=0.8L$ ; (c)  $L_m=1.2L$ ; (d)  $L_m=0.5L$ ; (e)  $L_m=1.5L$ .

To analyze the robustness of the proposed predictive current controller based on the Luenberger observer, the step response, impulse response and the closed-loop root locus analysis are performed when the different coupling inductance are considered. The obtained analytical results are shown in Fig.10, where the parameter  $L_m=L$ ,  $0.8L$ ,  $1.2L$ ,  $0.5L$ ,  $1.5L$ , respectively. Fig.10 shows that, the variation of  $L_m$  affects the closed-loop bandwidth and response time of the step response and impulse response.

When  $L_m$  reduces, the overshoot of the step response and impulse response also decreases and the system dynamics becomes sluggish. When  $L_m=0.5L$ , the overshoot equals to zero and the response time is 2.0ms. When  $L_m$  increases, the overshoot of the step response and impulse response increases and the system dynamic response is also enhanced. When  $L_m=1.5L$ , the overshoot equals to 0.6pu and the response time is 1.0 ms. It can be inferred that the closed-loop poles are always within the unit circle and the trajectory of the step response converges to unity under the parameter variations. These properties validate the excellent robustness of the devised current controller.

### III. Simulation Results Obtained from Matlab/Simulink

To validate the effectiveness of the control algorithms, the digital simulation of the CHB-APF is performed using the Matlab/Simulink software. The two-block inverter units are connected between the phase leg 'AB', 'BC' and 'CA'. The load is composed of three-phase diode rectifier with the ac-side inductance of 1mH to suppress the high  $di/dt$  ratio, and the dc-side resistance of  $R=4\Omega$  connected in parallel with the capacitance  $C=10000\mu F$ . The switching frequency of the IGBTs is set to be 2.5kHz, and the phase shift between the two inverter units across the same phase leg is set to be 90 degees [2, 6, 11-14].

The transient response of the CHB-APF is simulated by suddenly turning on the system for reactive and harmonic compensation of the nonlinear load. Besides, the dynamic response of the CHB-APF from the inductive mode to the capacitive mode is also simulated to test the robustness of the devised control algorithm, which are presented in the forthcoming subsections.

#### A. Transient Response of the Three-Phase CHB-APF

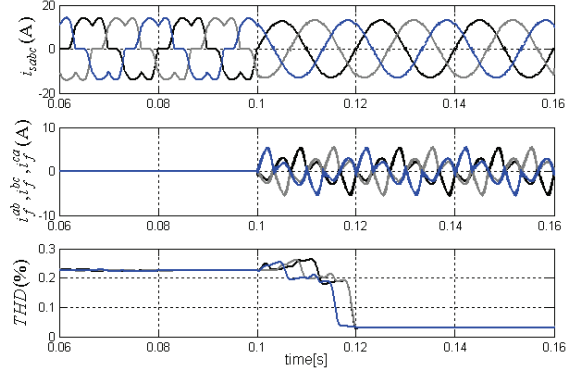


Fig.11 The transient response when the three-phase CHB-APF is suddenly turned on under the balanced nonlinear load scenario.

Figs.11-14 show the simulation results of the cascaded APF for the balanced nonlinear load compensation. The initial and the reference value for the dc-link capacitors of the CHB-APF are set to be 50V. It can be observed that the compensation currents of the CHB-APF track the reference command within half a cycle, and the sinusoidal grid currents are achieved at the source side with a unity power factor. The total harmonic distortion (THD) of the grid currents reduces from 22.45% to 2.08%, and the characteristic order harmonics are remarkably reduced.

For instance, the individual harmonic distortions of the fifth, seventh order harmonic are reduced from 20.8% and 7.5% to 1.16% and 1.2%, respectively, which complies with the power quality standard imposed by Std. IEEE 1992-519.

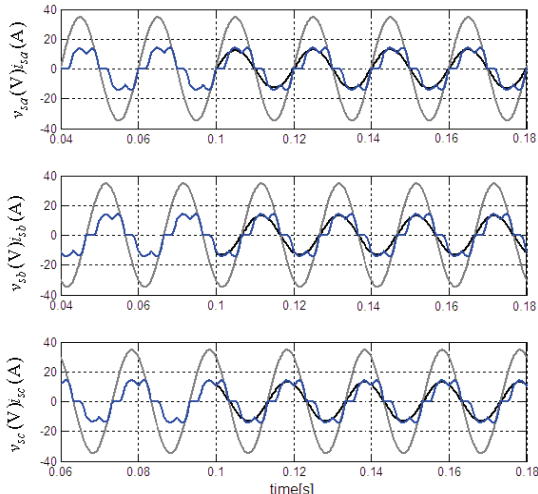


Fig.12 The transient response of the grid voltage and grid current when the three-phase CHB-APF is suddenly turned on.

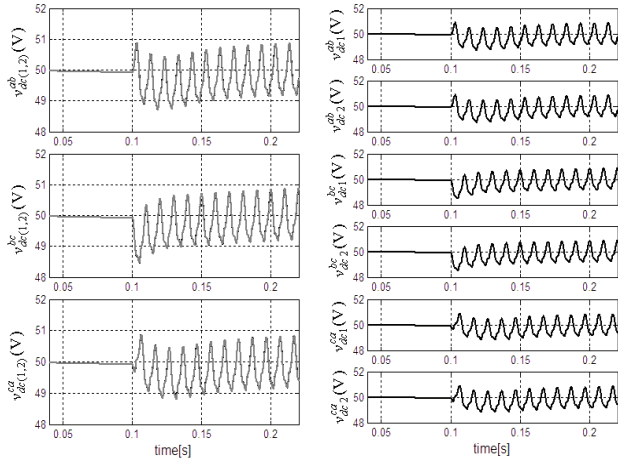


Fig.13 The transient response of dc-link voltages of the individual H-bridge inverter units when the CHB-APF is suddenly turned on.

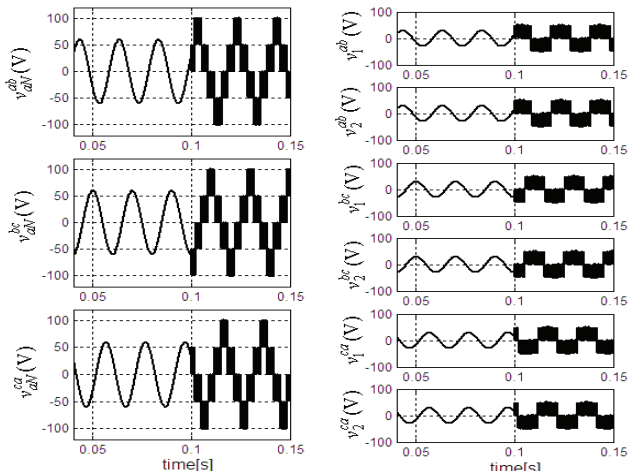


Fig.14 The transient response of the output voltages of the chain-link 'AB', 'BC', 'CA' and the individual H-bridge inverter units.

Fig.13 shows the dc-link voltages of the cascaded APF, it can be observed that the waveforms of the two inverters connected to the same phase overlap with each other, but the dc-link waveforms across the phase 'AB', 'BC', 'CA' are phase shifted by 120 degrees in the steady state. The dc-

link voltages are controlled to the reference voltage within one fundamental cycle, with a voltage ripple of 0.8V. Fig.14 shows the synthesized multilevel voltages of each phase leg and the ac-side voltage of the individual inverter unit. The three level voltages can be observed from the output voltages of each inverter unit, and the five level waveform can be observed from the synthesized multilevel voltages.

#### B. Dynamic Response of The Three-Phase CHB-APF from the Inductive Mode to the Capacitive Mode

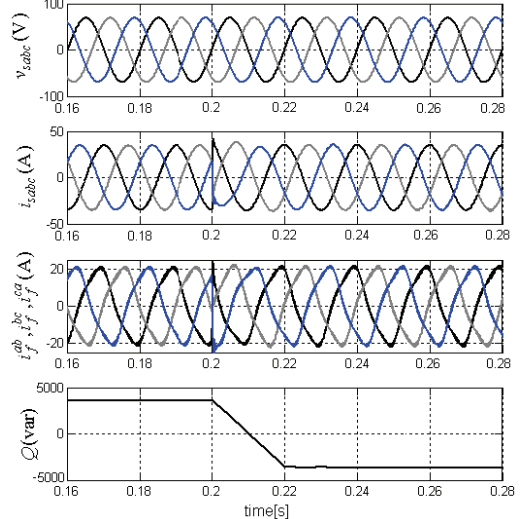


Fig.15 The transient response of grid voltage, grid current, CHB-APF current and the injected reactive power when the CHB-APF is operated from the inductive mode to the capacitive mode.

Figs.15-18 shows the dynamic response of the multilevel CHB-APF when it undergoes transition from the inductive mode to the capacitive mode. The CHB-APF generates a constant lagging reactive current of 20A when  $t < 0.2$ s, and generates a constant leading reactive current of 20A when  $t > 0.2$ s. The RMS value of the phase-to-phase grid voltage is set to be 60V, and the dc-link reference voltage is set to be 90V.

It can be observed from Fig.15 and Fig.16 that, the APF currents undergo 180 degrees phase angle jump when the reference currents are abruptly changed from inductive to capacitive at  $t=0.2$ s. Besides, the grid side currents also show 180 degrees phase angle jump at  $t=0.2$ s, and the grid currents are 90 degrees leading the grid voltages. The capacitive power changes from 4kVar to -4kVar within half a fundamental cycle, without any overshoot.

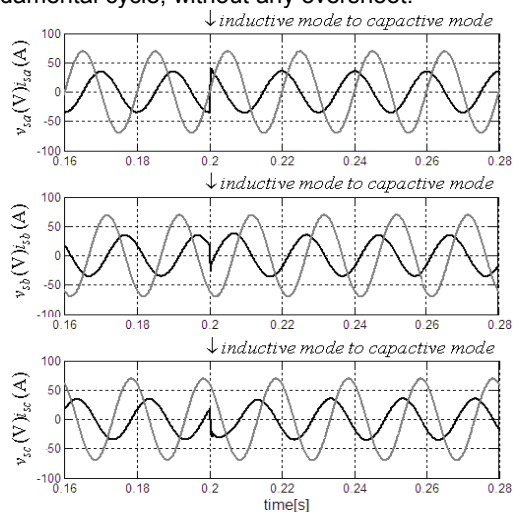


Fig.16 The transient response of the grid currents and voltages when the CHB-APF is under transition from the inductive mode to the capacitive mode.(Gray: grid voltages; Black: grid currents).

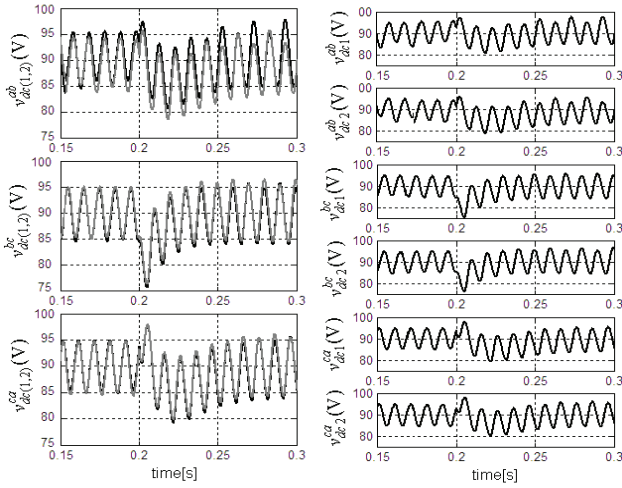


Fig.17 The individual dc-link voltages when CHB-APF is operated from the inductive mode to the capacitive mode.

It can be observed from Fig.17 that the dc-link voltages of the CHB-APF are controlled to the reference values in both the inductive and capacitive operation mode, with a voltage fluctuation of 5V. Moreover, the overshoot voltages are about 15V when the transition from the inductive mode to the capacitive mode is applied at  $t=0.2s$ . Fig.18 shows the transient response of the multilevel output voltage of each link and output voltages of the individual H-bridges. The five level output voltages can be observed from the ac-link voltages of each phase leg, and three level output voltages can be observed from the output voltages of the individual H-bridge modules. Notably, the convex-concave waveshapes can be observed from the multilevel voltages in the inductive and capacitive mode of the CHB-APF. And the phase angle of the grid current is lagging the multilevel output voltages by 90 degrees in case of inductive mode and leading the multilevel output voltages by 90 degrees in case of capacitive mode.

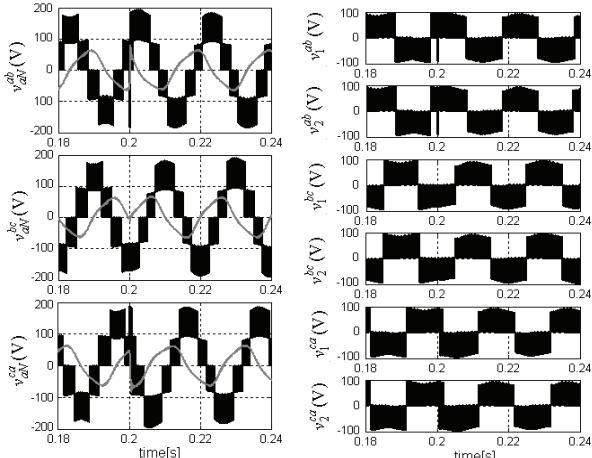


Fig.18 The transient response of the multilevel output voltages of each link and the output voltages of the individual H-bridge units.

#### IV. Control Algorithm Validation using EMTP-ATP

To further verify the effectiveness of the devised control algorithms for the three-phase CHB-APF, the simulation using the Electromagnetic Transient Program - Alternative Transient Program (EMTP-ATP) is also performed [5]. The Transient Analysis of Control System (TACS) and the MODELS language in the EMTP software are adopted to implement the control algorithm. The circuit parameters are: grid inductance  $L_s=50\mu H$ , the coupling inductance of the CHB-APF  $L=1mH$ , the dc-link capacitors of the CHB-APF  $C_{dc}=2000\mu F$ , and the load is composed of diode rectifier with  $RL$ -type load, and  $R_d=5\Omega$  and  $L_d=0.5 mH$ . The grid

voltages are set as 380V (phase to phase) and the target dc-link voltages are set as 400V.

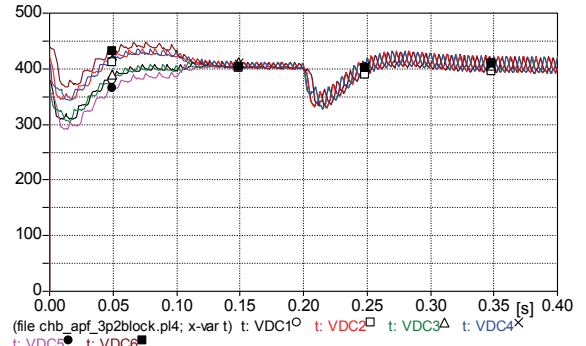


Fig.19 The dc-link voltages of the three-phase CHB-APF obtained from the electromagnetic transient program (EMTP-ATP).

Fig.19 shows the dc-link voltages of the multilevel CHB-APF obtained from the EMTP-ATP software. The voltages of the two inverters connected between phase 'A' and 'B' are indicated by 't: VDC1' and 't: VDC2'. The voltages of the two inverters connected between phase 'B' and 'C' are indicated by 't: VDC3' and 't: VDC4'. The voltages of the two inverters connected between phase 'C' and 'A' are indicated by 't: VDC5' and 't: VDC6'. The initial dc voltages are set to different values to test the convergence of the algorithm. The dc-link voltage balancing control algorithm can be found in the reference [11], which is omitted in this paper for the sake of brevity. The dc voltage balance controller is enabled at  $t=0.1s$ , and a transient increase of load is applied at  $t=0.2s$ . It can be observed that the dc link voltages converges to the preset values within a few cycles. The convergence speed can be dynamically adjusted by tuning the PI parameters in the voltage balancing controller (VBC), which was extensively discussed in [2, 3, 11].

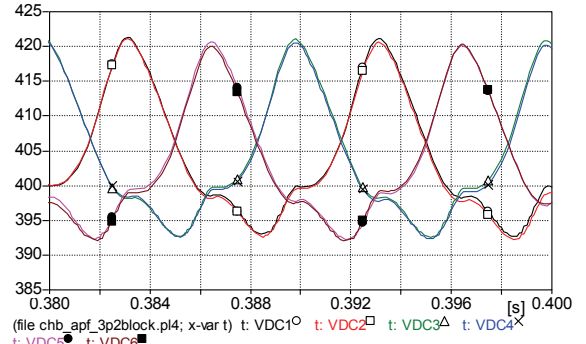


Fig.20 The enlarged view of the dc-link voltages of the CHB-APF.

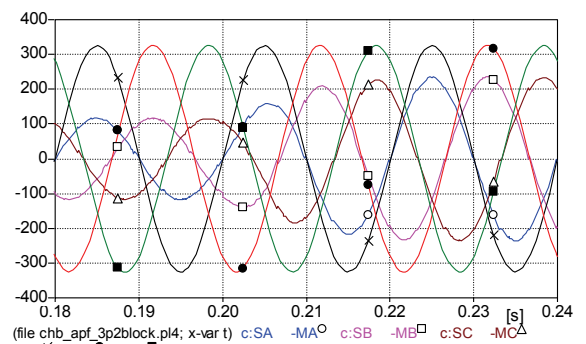


Fig.21 The grid voltages and currents obtained from EMTP-ATP.

Fig.20 shows the enlarged view of the dc-link voltages of the CHB-APF. The perfect matching of the dc-link voltages of the cascaded inverters across the same phase leg can be observed. Besides, phase displacement of 120

degrees can also be observed among the dc-link voltages of the chain-link 'AB', 'BC' and 'CA'. Fig.21 shows the grid currents and grid voltages obtained from the EMTP-ATP software. Fig.22 shows the load currents, the currents between each phase leg of CHB-APF with respect to grid current and voltage in phase 'A'. It can be observed from Fig.21 and Fig.22 that the grid side currents are controlled in phase with grid voltages, thus the unity power factor is achieved at the grid side. Moreover, sufficient steady state precision and fast dynamic response is achieved, which validates the effectiveness of the devised control algorithm.

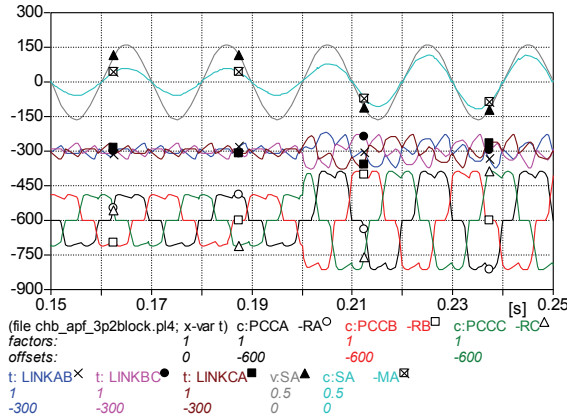


Fig.22 The load currents and currents between each phase leg of CHB-APF with respect to the grid current and voltage in phase 'A'.

From the extensive simulation results obtained from the EMTP-ATP and Matlab/Simulink, it can be concluded that the devised control algorithm is quite effective for reactive and harmonic compensation for the nonlinear load, which can also be applied for other grid-connected converters.

## V. Conclusions

This paper presents modelling and controller design for the three-phase cascaded H-bridge multilevel APF. The mathematical model is derived using state space equations, and the discrete domain model is also derived. A robust current controller of CHB-APF is proposed, which is based on the Luenberger observer with the characteristics of the two beat predictive current controller. The performance of the current controller is evaluated, and the effect of control delay is also taken into account. The system robustness is analyzed with control delay under parameter variations of the coupling inductance. Finally, simulation results from the Matlab/Simulink and EMTP-ATP softwares are presented, which verifies the validity and effectiveness of the devised control algorithms.

## ACKNOWLEDGEMENT

This project is supported by the Fundamental Research Funds for the Central Universities (No. ZYGX2011J093).

## REFERENCES

- [1] Biricik S., Ozerdem O., Investigation of switched capacitors effect on harmonic distortion levels and performance analysis with active power filter, *Przeglad Elektrot.*, 85(2010), n.11a, 13-17.
- [2] Han Y., Xu L., Yao G., Zhou L., Khan MM, Chen C., State-Space Averaging (SSA) Technique for Modeling of the Cascaded H-Bridge Multilevel DSTATCOMs and Active Filters, *International Review of Electrical Engineering-IREE*, 4(2010), n.5, 744-760.
- [3] Brahim B., Chellali B., Mostefa R., Hamza T., An efficient algorithm to tuning PI-controller parameters for shunt active power filter using ant colony optimization, *Przeglad Elektrot.*, 87(2011), n. 6, 140-145.
- [4] Han Y., Xu L., A survey of the smart grid technologies: background, motivation and practical applications, *Przeglad Elektrot.*, 87(2011), n.6, 47-57.
- [5] Han Y., Xu L., Yao G., Zhou L., Khan MM, Chen C., Flicker mitigation of arc furnace load using modified p-q-r method, *Przeglad Elektrot.*, 85(2009), n.1, 225-229.
- [6] Han Y., Xu L., Yao G., Zhou LD., Khan MM., Chen C., A novel modulation scheme for dc-voltage balancing control of cascaded H-bridge multilevel APF, *Przeglad Elektrot.*, 85(2009), n. 5, 81-85.
- [7] Tomasz A., Dawid B., Marian P., Simulation of active power filter with prediction control in Matlab and Orcad environments with using SLPS interface, *Przeglad Elektrot.*, 87(2011), n. 5, 1-5.
- [8] Han Y., Xu L., Yao G., Zhou L., Khan MM, Chen C., A Robust Deadbeat Control Scheme for Active Power Filter with LCL Input Filter, *Przeglad Elektrot.*, 86(2010), n.2, 14-19.
- [9] Han Y., Xu L., Khan MM, Chen C., Yao G., Zhou L., Modelling and controller synthesis of a hybrid-LCL APF for power quality conditioning applications, *Przeglad Elektrot.*, 86(2010), n.9, 326-333.
- [10] Kazimierz M., Andrzej T., Ripple estimation in active power filters, *Przeglad Elektrot.*, 87(2011), n.5, 111-115.
- [11] Han Y., Xu L., Khan MM, Chen C., Power balancing control strategies for the cascaded H-bridge multilevel DSTATCOM, *Przeglad Elektrot.*, 87(2011), n.2, 212-219.
- [12] Sergio V., Jose IL., Juan M.C., Leopoldo GF., etc., Analysis of the power balance in the cells of a multilevel cascaded H-bridge converter, *IEEE Trans. Ind. Electron.*, 57(2010), n.7, 2287-2296.
- [13] Barrena J., Marroyo L., Vidal M., Apraiz J., Individual voltage balancing strategy for PWM cascaded H-bridge converter-based STATCOM, *IEEE Trans. Ind. Electron.*, 55(2008), n.1, 21-29.
- [14] Han Y., Xu L., Averaged and switching function modelling for the active power filter with LCL-type coupling impedance, *Przeglad Elektrot.*, 87(2011), n.4, 176-181.
- [15] Krzysztof S., Control circuit for active power filter with an instantaneous reactive power control algorithm modification, *Przeglad Elektrot.*, 87(2011), n.1, 96-100.

**Authors:** Dr. Yang Han is with the Department of Power Electronics, School of Mechatronics Engineering, University of Electronic Science and Technology of China (UESTC), No.2006 XiYuan Road, West Park of Chengdu High-Tech Zone, Chengdu, China, 611731, E-mail: [hanyang\\_facts@hotmail.com](mailto:hanyang_facts@hotmail.com);